Massive collapse of two glaciers in western Tibet in 2016 after surge-like instability

Andreas Kääb[1]*, Silvan Leinss[2], Adrien Gilbert[1], Yves Bühler [3], Simon Gascoin [4], Stephen G. Evans[5], Perry Bartelt[3], Etienne Berthier [6], Fanny Brun [6,7], Wei-An Chao[8], Daniel Farinotti[9,10], Florent Gimbert[7], Wanqin Guo[11], Christian Huggel[12], Jeffrey S. Kargel[13], Gregory J. Leonard[14], Lide Tian[15], Désirée Treichler[1] and Tandong Yao[15]

Surges and glacier avalanches are expressions of glacier instability, and among the most dramatic phenomena in the mountain cryosphere. Until now, the catastrophic collapse of a glacier, combining the large volume of surges and mobility of ice avalanches, has been reported only for the 2002 $130 \times 10^6\,\text{m}^3$ detachment of Kolka Glacier (Caucasus Mountains), which has been considered a globally singular event. Here, we report on the similar detachment of the entire lower parts of two adjacent glaciers in western Tibet in July and September 2016, leading to an unprecedented pair of giant low-angle ice avalanches with volumes of $68 \pm 2 \times 10^6\,\text{m}^3$ and $83 \pm 2 \times 10^6\,\text{m}^3$. On the basis of satellite remote sensing, numerical modelling and field investigations, we find that the twin collapses were caused by climate- and weather-driven external forcing, acting on specific poly-thermal and soft-bed glacier properties. These factors converged to produce surge-like enhancement of driving stresses and massively reduced basal friction connected to subglacial water and fine-grained bed lithology, to eventually exceed collapse thresholds in resisting forces of the tongues frozen to their bed. Our findings show that large catastrophic instabilities of low-angle glaciers can happen under rare circumstances without historical precedent.

Sudden, gravity-driven mass failures of glaciers have been observed over a wide range of magnitudes, from ice falls at steep glacier fronts to large ice avalanches when hanging glaciers, typically steeper than 30°, detach[1,2]. Impacts are mostly within a couple of kilometres, except when the ice transforms to a highly mobile mass flow through ingestion and production of melt water and incorporation of sediments[3,4]. Pre-failure conditions and triggering factors typically include topographic, atmospheric and ice-thermal conditions[1,2], underlying bedrock instabilities or seismic events[3,5].

Glacier surges constitute a second process of glacier instability and refer to events lasting weeks to a few years with abnormally high flow speeds of up to tens to hundreds of metres per day over large glacier parts[6–10]. Clusters of surge-type glaciers are found in mountain regions around the world, including the Tibetan Plateau[7,9,11]. Processes involved in the lowering of basal friction required for surging include abnormally high water pressure[8,11,12], change in the thermal regime[10,11,13,14] and complex responses of subglacial till rheology to increasing shear stress and water input[6,8,11,12,15–17].

A third type of glacier instability involves the detachment of large parts of low-angle valley glaciers. This process has been documented only for the 2002 Kolka Glacier event (Kazbek massif, Caucasus), when a $130 \times 10^6\,\text{m}^3$ ice/rock avalanche travelled 18 km down-valley and claimed 120 lives[18–20]. The massive 2016 glacier collapses in Tibet[21] have changed this picture and opened

up critical questions about the causes of the detachments and the potential for similar events to occur elsewhere. Here, we describe the Tibet twin events and reconstruct the evolution of the collapsed glaciers since the 1960s, on the basis of remote sensing and mass-balance modelling. For more recent years, we analyse glacier dynamics and model the thermal conditions to infer details about the glacier's stress and frictional regime. Finally, we discuss the influences of melt and precipitation, bed lithology and glacier geometry on the collapses.

From glacier collapses to high-speed avalanches

On 17 July 2016, 11:15 Beijing time, a massive volume of glacier ice detached from the lower part (5,800–5,190 m a.s.l.) of an unnamed glacier in the Aru Range (Rutok County, China) in the western Tibetan Plateau (termed Aru-1 for both glacier and collapse; Figs. 1 and 2). The fragmented ice mass ran out 6 km beyond the glacier terminus, killing nine herders and hundreds of their animals, and reached the Aru Co lake[21] (~4,970 m a.s.l.; Fig. 1). The avalanche horizontal distance of 8.2 km and its vertical path of 800 m yield a surprisingly low angle of reach of only 5–6° (mobility index fahrböschung[22]), indicating very low basal friction in the movement. The ice debris covered 8–9 km² and using pre/post-collapse differencing of digital elevation models (DEMs), a volume of the detached glacier part of $68 \pm 2 \times 10^6\,\text{m}^3$ was calculated (Fig. 2; Methods). The avalanche generated an impact wave, which

[1]Department of Geosciences, University of Oslo, Oslo, Norway. [2]Institute of Environmental Engineering, ETH Zurich, Zurich, Switzerland. [3]WSL Institute for Snow and Avalanche Research SLF, Davos Dorf, Switzerland. [4]CESBIO, CNES, CNRS, IRD, UPS, Université de Toulouse, Toulouse, France. [5]Department of Earth and Environmental Sciences, University of Waterloo, Waterloo, ON, Canada. [6]LEGOS, CNES, CNRS, IRD, UPS, Université de Toulouse, Toulouse, France. [7]CNRS, IRD, Grenoble INP, IGE, Univ. Grenoble Alpes, Grenoble, France. [8]Department of Civil Engineering, National Chiao Tung University, Hsinchu, Taiwan. [9]Laboratory of Hydraulics, Hydrology and Glaciology, ETH Zurich, Zurich, Switzerland. [10]Swiss Federal Institute for Forest, Snow and Landscape Research (WSL), Birmensdorf, Switzerland. [11]Northwest Institute of Eco-Environment and Resources, Chinese Academy of Sciences, Lanzhou, Gansu, China. [12]Department of Geography, University of Zurich, Zurich, Switzerland. [13]Department of Hydrology and Atmospheric Sciences, and Planetary Science Institute, University of Arizona, Tucson, AZ, USA. [14]Lunar and Planetary Laboratory, University of Arizona, Tucson, AZ, USA. [15]Institute of Tibetan Research, Chinese Academy of Sciences, Beijing, China. *e-mail: kaeaeb@geo.uio.no
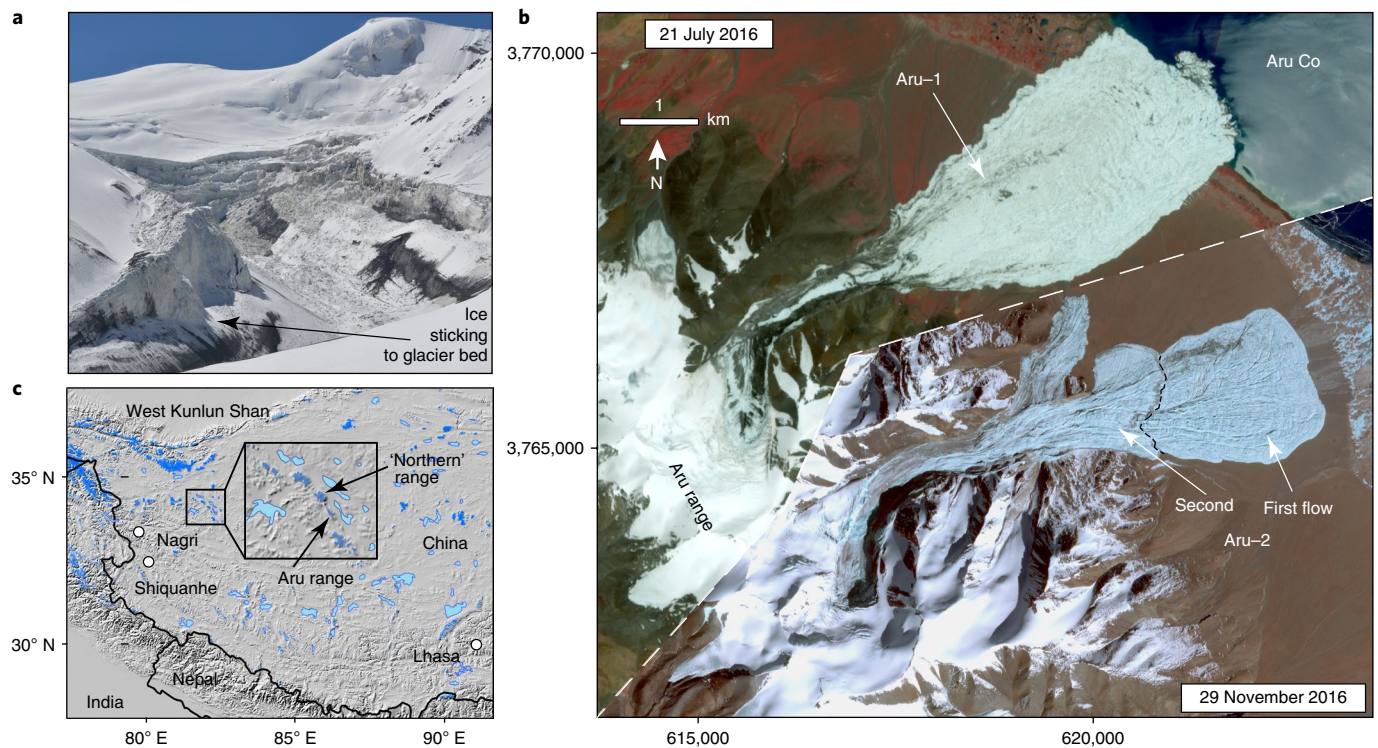
Fig. 1 | Satellite and terrestrial images of the Aru glacier collapses. a, A photo of the upper Aru-2 detachment zone (4 October 2016). **b**, A mosaic of a Sentinel-2 image of Aru-1 collapse (21 July 2016) and a Planet image of Aru-2 collapse (29 November 2016); coordinates: metres in WGS84 UTM zone 44; the image centre is approximately 34.03° N/82.28° E. **c**, An overview of the study region with the meteorological stations used.

inundated the opposite shore of Aru Co over a shoreline distance of 10 km, extending up to 240 m inland and 9 m above lake level (Methods and Supplementary Section 11).

In a dramatic turn of events, on 21 September 2016, a second glacier (Aru-2) detached just 2.6 km south of the July event. The detachment occurred at 5,800–5,240 m a.s.l. in two main flows at about 5:00 and 11:20 Beijing time (Figs. 1 and 2). Similarly to the July event, the glacier mass fragmented and transformed into a mass flow that ran out 5 km beyond the glacier terminus, reaching 4,965 m a.s.l. Over a horizontal distance of 7.2 km, the vertical height of the path was 830 m, giving a similarly low fahrböschung of 6–7°. The glacier debris in the second collapse covered 6–7 km² with a detached glacier volume of $83 \pm 2 \times 10^6$ m³ (Fig. 2).

Eyewitness reports, the geomorphology of the avalanche paths and deposits, and observations of seismic waveforms generated by the mass movements all suggest that the events were sudden and fast (2–3 min duration, 30–40 m s⁻¹ mean speed; Supplementary Section 10). Consistent with the low basal friction estimated from the avalanche paths, the analysis of the three-dimensional forces inverted from the glacier avalanche seismic signals[23] also reveals exceptionally low basal friction coefficients of 0.11 ± 0.07 and 0.14 ± 0.05 for Aru-1 and 2, respectively (ratio between frictional and normal force; Supplementary Section 10). These values are significantly smaller than values on the order of 0.2–0.6 previously found for landslides. Using different numerical avalanche flow models[24,25], we find average flow speeds of ~20 m s⁻¹, peaking at 70–90 m s⁻¹ in the gorge sections of the paths. High avalanche speeds are also indicated by the presence of undestroyed grassy vegetation on the lee side of hills in the Aru-1 avalanche path, suggesting that the fast-moving mass had partially jumped over it[19] (Supplementary Section 1). The high speeds for both Aru avalanches suggest processes of ice liquefaction from frictional heating during the collapse and flow[26]. From simple energy conservation,

up to 2.3% of the ice could have liquefied if all potential energy was consumed, with the generated water probably concentrated at the bed of the flow.

Prior to the Aru-2 collapse, crevasses very similar to the ones preceding the Aru-1 event were detected on satellite imagery (Fig. 3f), the potential avalanche run-out geometry and general deposition pattern were modelled with the parameters inferred from the Aru-1 simulation, and an alert was issued to Chinese authorities.

Climate and glacier changes from 1961 to 2016

We investigate recent climate and meteorological records in the Aru region to identify possible pre-conditions and triggers for the two glacier collapses. The Shiquanhe meteorological station (Fig. 1), providing the closest long-term record, reveals strong warming of 1.7 ± 0.5 °C since 1965 (Supplementary Section 3), in line with reductions in glacier length in the western Tibetan Plateau[27,28]. Precipitation at Shiquanhe does not show a long-term trend, but exceptionally large precipitation sums occurred in 2013 and 2015, and in 2016 at the Nagri station (established in 2010).

Using Corona satellite imagery over the period 1961–1980, Landsat from 1972 on, and high-resolution optical and radar satellites from 2011 to date, we find that the glaciers in the Aru Range retreated from the 1970s on; Aru-1 and Aru-2 glaciers by 520 and 460 ± 15 m between 1970 and 2015 or 2016, respectively. In contrast to this frontal retreat, analysis of DEMs from SRTM-X (2000), TanDEM-X (2011–2016) and the Advanced Spaceborne Thermal Emission and Reflection Radiometer[29] (ASTER; 2000–2015; Methods), together with ICESat laser altimetry[30] (2003–2008), show that glaciers in the wider Aru region are part of the Karakoram, Kulun Shan and Eastern Pamir anomaly[29,30] and experienced a slight thickness increase of between 0.20 ± 0.16 and 0.28 ± 0.15 m yr⁻¹ water equivalent (w.e.) since the early 2000s (ASTER and ICESat,
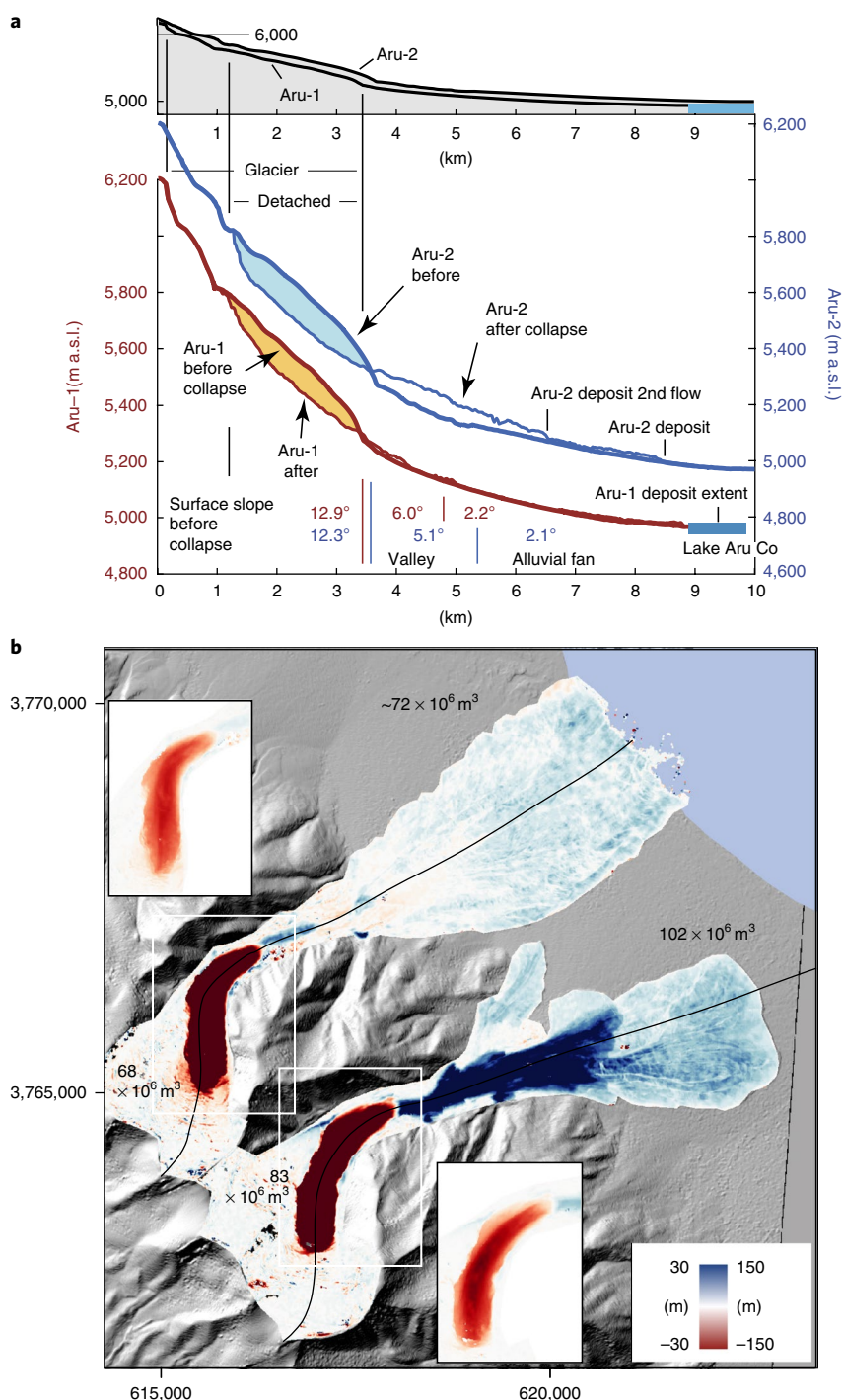
Fig. 2 | Geometry and thicknesses of the Aru collapses and avalanches. a, Longitudinal profiles over the collapses and avalanche deposits without and with vertical exaggeration. The profile location is shown in **b**. **b,** Elevation changes between 25 November 2015 (SPOT7, outside glaciers merged with TanDEM-X) and 1 October 2016 (Pléiades). The collapse source zones are given in two colour scales (±30 m, main figure; ±150 m, insets). Note the distinct steps of deposit thickness between the upper and lower parts of the Aru-2 mass-flow deposits and within the lower part. The numbers in the panel indicate source and deposit volumes.

respectively; Fig. 4). Simultaneous high-elevation thickening and low-elevation thinning and terminus retreat causes steepening of the glacier surface and is generally untypical. However, for non-surge-type glaciers, it has been observed when both temperature and snowfall increase together[31], causing increased ice melt and accumulation. Specifically, non-surging glaciers in the Aru region thickened by up to $0.40 \pm 0.15\,\mathrm{m\,yr^{-1}}$ above around 5,650 m a.s.l.

and thinned up to $1.20 \pm 0.15\,\mathrm{m\,yr^{-1}}$ below that elevation (Fig. 5a). For at least 5 of 16 glaciers in the range north of the Aru Range, this overall climate-driven pattern of surface elevation changes was interrupted by surge-type mass redistributions over 2000–2016 (Supplementary Section 7).

Despite regional warming, mass-balance modelling of the Aru glaciers (Fig. 4, Methods and Supplementary Section 3) confirms
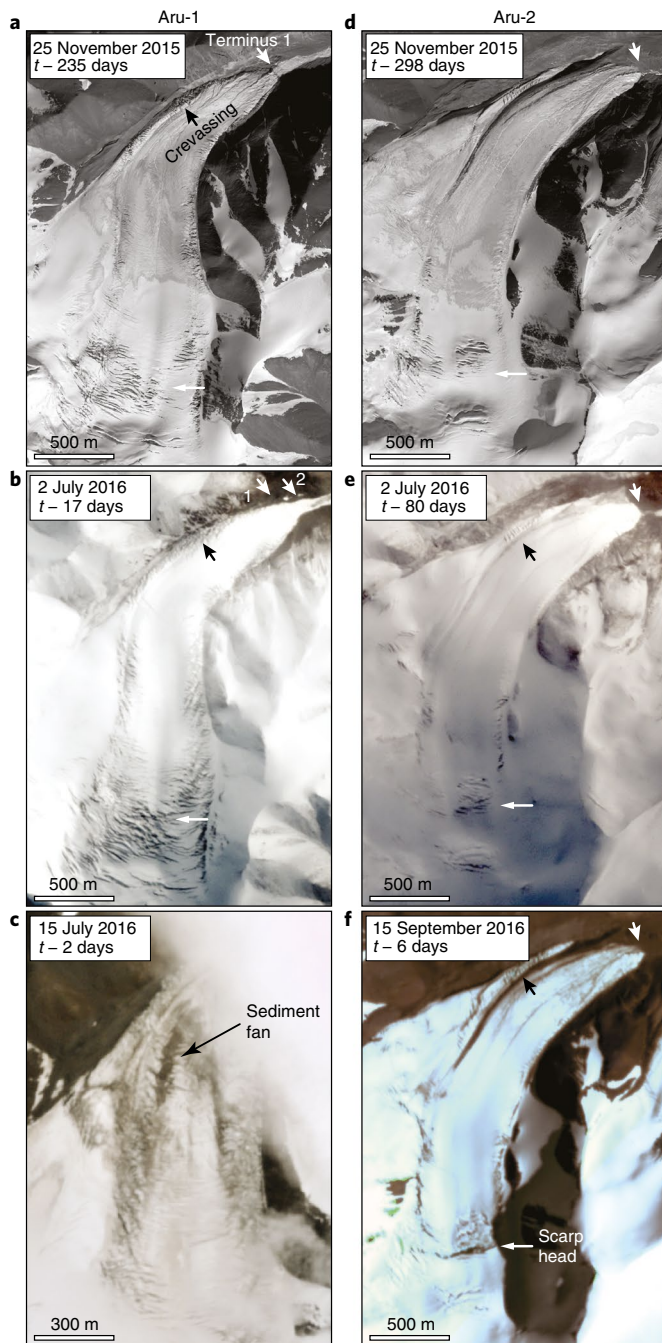
Fig. 3 | Satellite images over the Aru glaciers before collapse. a, Aru-1 glacier (SPOT7, Airbus). Time *t* refers to collapse date. The glacier front position is indicated by arrow 1. Note the particular crevassing at the northern curve of the glacier. **b**, Aru-1 (Planet). The glacier front was at arrow 2. **c**, Aru-1 (Planet). A sediment fan on the glacier surface two days before collapse originated from a crevasse. The image in **c** is slightly zoomed in. **d**, Aru-2 (SPOT7, Airbus). **e**, Aru-2 (Planet). **f**, Aru-2 (Planet), six days before collapse. The horizontal arrow indicates the scarp head positions of the later detachments.
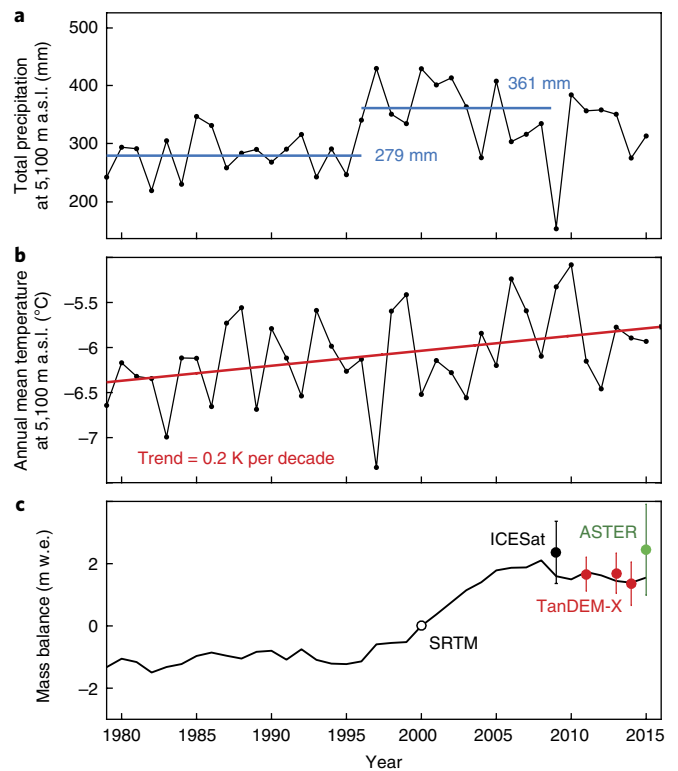

Fig. 4 | Climatic data series and modelled mass balance of the Aru glaciers. a, Precipitation over the Aru Range from ERA-interim reanalysis, suggesting a distinct increase at around 1995. The bold lines are averages for 1979–1995 and 1995–2008. **b**, Air temperature over the Aru Range from ERA-interim reanalysis with a positive trend of $0.2 \pm 0.1\,K\,10\,yr^{-1}$. **c**, Modelled cumulative glacier water equivalent (w.e.) mass balance of the Aru glaciers, driven by ERA-interim reanalysis. The model is relative to the year 2000 (SRTM DEM), and the parameters were tuned using geodetic mass balances (ICESat, 2003–2008; SRTM-X versus TanDEM-X, 2000–2011/2013/2014; ASTER, 2000–2015, end points indicated).

Searching the Corona (from 1961) and Landsat (from 1972) archives, we find no indication of earlier glacier collapses in the Aru Range and its wider region (radius of about 300 km). However, we note that early Corona images and 2015/2016 satellite data for the two Aru glaciers and some of their close neighbours show similar strong crevassing and bulged tongues; that is, features commonly presaging surge-like instabilities or rapid advance (Supplementary Section 1).

Pre-collapse mass redistribution within polythermal glaciers
Patterns of glacier-surface elevation changes in the immediate pre-collapse period (2011–2015) are measured from repeat TanDEM-X DEMs and optical satellite stereo DEMs (Fig. 5b,c; Methods and Supplementary Section 7). At least as early as 2011 and until 2014, the sections above the eventual detachment zones of both Aru glaciers at ~5,800 m subsided. Simultaneously, glacier sections ~5,800–5,400 m a.s.l. bulged upwards. Combined with thickness loss at the termini ~5,400–5,200 m a.s.l., the bulging led to steepening by 5–6° at its front, and thus to locally increasing driving stresses. The elevation change rates derived for 2011–2014 indicate that a down-glacier mass transfer had begun already 2003 ± 3 yr (Supplementary Section 7). However, this internal mass movement did not cause surging of Aru-1 before mid-2015 and only 200 ± 15 m terminus advance up to collapse, whilst no advance was detected for Aru-2 at all (Fig. 3). These observations indicate strong resistive forces to sliding at the glacier termini, suggesting that they were frozen to their beds[14].

positive mass balances between 1995 and 2008, and steepening of the mass-balance gradient. We attribute this to a precipitation increase since the mid-1990s[32,33] captured by the ERA-interim reanalysis that drives our model. This precipitation increase is confirmed by wide-spread growth of the region's endorheic lakes during the same period[34].
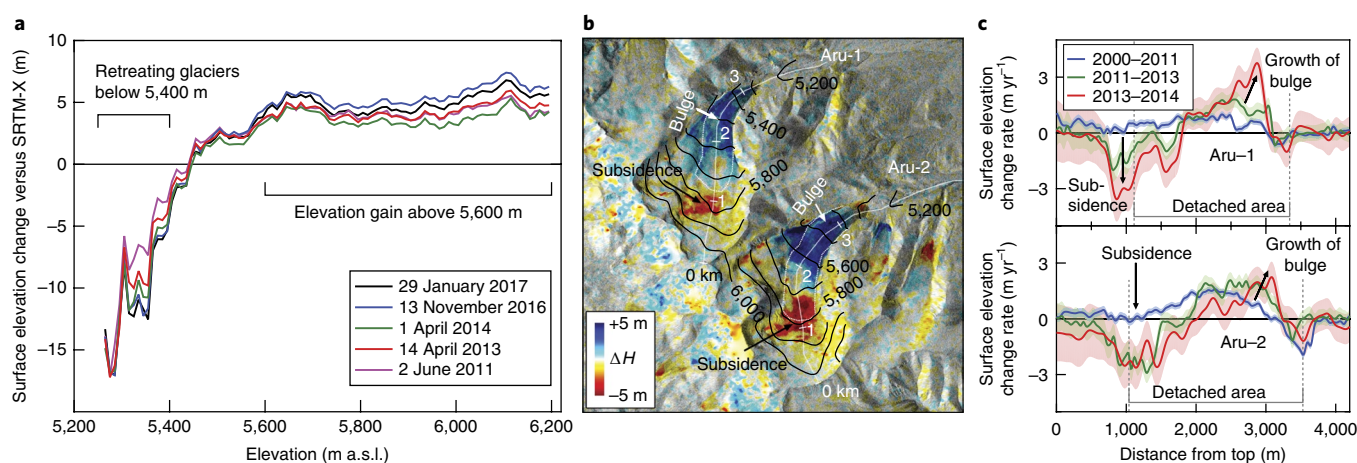
Fig. 5 | Glacier thickness changes over the Aru region and Aru glaciers since 2000. a, Glacier surface elevation changes between SRTM-X (2000) and various TanDEM-X DEM dates over non-surging glaciers plotted against elevation. **b**, TanDEM-X-derived surface elevation change (ΔH) map between June 2011 and April 2013. **c**, SRTM-X and TanDEM-X surface elevation change rates over Aru glacier profiles (in **b**) showing bulging and bulge propagation over the period 2000–2014. Simultaneous bulge growth and frontal thinning/retreat steepens the glacier front. The line shading indicates one standard deviation uncertainty.

Image offset-tracking reveals that the Aru-1 medial bulge was associated with increased ice velocities, from $0.18 \pm 0.03\,\text{m}\,\text{d}^{-1}$ in late 2013, to $0.50 \pm 0.04\,\text{m}\,\text{d}^{-1}$ in spring 2016 (Supplementary Section 8). These are 3–10 times higher flow speeds compared with the modelled steady-state flow of $0.05\,\text{m}\,\text{d}^{-1}$ (Methods). For the Aru-2 glacier, we find unchanged average central speeds in the medial bulge of $0.12 \pm 0.03\,\text{m}\,\text{d}^{-1}$ between July 2013 and April 2016.

Strongly enhanced crevassing developed on both glaciers in the weeks to months before the detachments (Fig. 3). Crevassing was particularly evident along the lateral margins and across the glaciers at an elevation of ~5,800 m a.s.l., indicating increased displacement where the glaciers later detached. On Aru-1, cracks across the entire glacier had already evolved in September 2015 (Supplementary 1). Fast-developing crevasses on Aru-2 were discovered in satellite images before its collapse.

The high initial acceleration of the avalanches, the pattern of glacier surface height changes, thermo-mechanical modelling of the glaciers outlined below, and the crevasse formation indicate that enhanced basal sliding first occurred in the central parts of the glaciers. The presence of large amounts of water is also suggested by a mudflow-like fan of basal fines originating at around 5,550 m a.s.l. from crevasses, which is observed on satellite images of Aru-1 from two days before its collapse (Fig. 3). No such observation was made for Aru-2.

Thermo-mechanical modelling (Methods) indicates that the ice/bed interface was probably temperate (thawed) in the central part of the glaciers but cold (frozen) in the remaining zones (Fig. 6), suggesting a polythermal structure for the Aru glaciers. The model-indicated thermal patterns are supported by the late (Aru-1) or missing (Aru-2) advances of the fronts, significant ice masses sticking at the glacier margins after detachment (Fig. 1), and the location of the Aru range within a semi-arid permafrost region[35]. The polythermal glacier structure created conditions for: margins and fronts of the glacier tongues to be frozen to the underlying bed; infiltrating melt water to reach the glacier bed at the top of the detachment zones; the retention of this water upslope of the cold-based plugs creating the precursory friction decrease within the medial bulges[17]; and the development of a progressively steepening geometry upstream of the cold-based fronts. Critically, the cold-based front prevented the glacier geometry from adapting quickly enough to the reduction in friction, as would be the case during typical surges. The accumulation of water at the glacier bed through ingress of rainfall and in par-
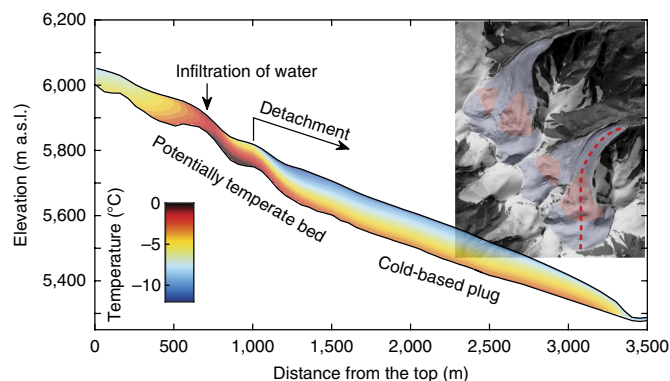

Fig. 6 | Modelled two-dimensional thermal structure of the Aru glaciers. Median scenario of a suite of thermodynamic steady-state flow-line modelling results of the thermal structure of Aru-2 for the mean 1980–1995 climate conditions. The models indicate temperate (thawed) basal conditions at the position of the later scarp head and under the upper zone of the detached glacier part, and otherwise cold (frozen) basal conditions. The results for Aru-1 are very similar and not shown. Inset, schematic representation of the basal temperature of the Aru glaciers at steady state. The areas in blue are probably cold-based ice; the areas in red are potentially temperate-based ice.

ticular summer melt was probably accelerated after 2010 when the sum of both contributions increased by ~50% (Supplementary Sections 3 and 4).

Causes and implications

No earthquake seismicity was associated with the initiation of either event (Methods). Global Precipitation Measurement Integrated Multi-Satellite Retrievals (GPM IMERG) and the meteorological stations in the region indicate significant amounts of precipitation throughout the summer of 2016 of up to 200 mm or more in total. For the two days immediately preceding the Aru-1 collapse, 10–25 mm rainfall was observed (Supplementary Section 6). Optical satellite images reveal considerable rates of snow-cover reduction in the weeks before the collapse. Very low backscatter in Sentinel-1 radar data from 1 July until 31 August 2016 indicates

continued melting conditions up to the mountain tops of the Aru Range (~6,100 m a.s.l.; Supplementary Section 4). No similar strong precipitation is observed for the days immediately preceding the Aru-2 event, although several rainfall events occurred during the weeks prior to collapse. Hence, at least for Aru-1, unusually high liquid water input from melting and precipitation (highest positive degree-day sum since 1979 found for 2016; Supplementary Section 3) increased the water content in the glacier system, and thus puts it among the possible triggering factors for the collapse.

An important factor relates to the deformable bed[6,8,15,16,36,37] of the Aru glaciers, linked to the fine-grained sandstone and siltstone (possibly lightly metamorphosed) that is mapped underneath the collapsed Aru glaciers, and to clay-rich till, which we sampled (Methods). We suggest that on commencement of basal thaw and sliding, the till formed from these lithologies, combined with the high water input, may have locally formed basal slurries with low shear strength under high pore-fluid pressure[38], and possibly have destroyed any subglacial drainage system[17]. The limited strength of the till in those areas would have induced a rheology prone to trigger instabilities[39,40].

The curved shape in plan geometry of the two glacier tongues might also have influenced their stability by causing lateral resistance[8]. This is indicated by strong crevassing (Fig. 3) and maximum flow speeds at the northern, left-lateral glacier margins (Supplementary Section 8). We also note that the surface slopes of 12–13° (bed slopes 9–10°) of the detached avalanche sources rank rather high for surge-type glacier tongues, thus exerting high driving stresses[8].

In sum, the foregoing shows that there is no evidence for a single trigger for the twin collapses. The surge-like behaviour, climate-driven glacier surface steepening, polythermal glacier structure, their geometry and slope, and liquid water from melt and rain during summer 2016 are all factors found for a number of other glaciers both on the Tibetan Plateau and elsewhere. We propose therefore that a transient convergence of factors acting at different spatial and temporal scales caused the Aru collapses. A polythermal glacier regime, glacier morphology and bedrock lithology represent important basic conditions. Over timescales of 15–20 years, the simultaneous increase in temperature and precipitation has acted on the glacier geometry and basal friction by respectively increasing the slope and enhancing liquid-water input to the glacier bed, and possibly expanding the area of thawed conditions. The presence of cold-based fronts and margins prevented the glaciers from adjusting their geometries to changed driving stresses and frictional conditions. This continuously increased the stresses on the frozen terminus and margins, until reaching a critical point for which the resisting forces were eventually overcome and the collapses occurred. The sustained exceptional low frictions over large parts of the glaciers make the events unique and are probably associated with a particular response of the fine-grained basal till to large amounts of liquid water[6,8,17,41]. The final trigger is thought to be linked to short-term variation in the subglacial hydrological system induced by the unusually high water input from melt and rain in the summer of 2016. Hydro-thermodynamic feedback[42] potentially played a role as well—a mechanism by which water reaching the glacier bed through crevasses increases basal sliding, strain and associated fracturing through a combination of thermal and dynamic changes, thus facilitating additional water input and modifying subglacial drainage[43].

Some similarities exist between the 2016 Aru events and the 2002 Kolka Glacier collapse including volume, glacier and avalanche slopes, and avalanche speed. In the days before detachment[18–20], Kolka Glacier showed signs of destabilization including heavy crevassing and bulging, and unusual hydrological conditions[43] such as supraglacial ponds. This glacier surged in 1969/1970[19] and had a slope similar to the two Aru glaciers[18]. The Kolka/Kazbek area is known for its fine-grained rocks and sediments of volcanic origin[44] causing a variety of violent mass movements[45], and putting forward the possible role of lithology in the rapid and sustained reduction of basal friction in the three events. Unusually high geothermal heat fluxes underneath the Kolka[44] and Aru glaciers (Methods) are uncertain but cannot be excluded. In contrast to the Aru glaciers, however, Kolka Glacier must have been temperate throughout. Over some weeks before the event, moreover, heavy rock/ice-fall activity deposited several million cubic metres of material on the glacier[18–20]. The Kolka and Aru cases together suggest thus two possibilities to reach critical glacier geometry and associated increase in driving stresses; that is, additional loading from surrounding mass movements (Kolka) or glacier steepening (Aru).

In conclusion, the Aru twin glacier collapses have allowed us to recognize a new form of glacier instability—the catastrophic collapse of large parts (here ~25–30% by area, and up to 40% by volume) of an entire valley glacier. These collapses seem possible through a rare but not unique array of factors that coalesce to an anomalous increase in driving stresses, and rapid and sustained reduction of basal friction. It is spectacular and completely unprecedented that such combined exceedance of stability thresholds, highly unlikely for one glacier alone, occurred for two neighbouring glaciers within just two months. Rock-mechanical or hydrologic/hydraulic collateral effects through which the Aru-1 collapse could have preconditioned or triggered Aru-2 appear implausible, highlighting the role of common external forcing by climate and weather in synchronizing the two collapses. Our findings shed new light on the occurrence of glacier surge-related instabilities; several documented glacier instabilities[46–50] should be revisited to clarify their relation to the processes of glacier collapse suggested here. The transient nature of some of the factors involved in the Aru and Kolka collapses, and the range of conditions and thresholds suggested by the differences between them, imply that such events can happen without historical precedent. Once the Aru avalanche deposits have melted, their geomorphic and lithologic imprint should be investigated and the wider region be searched for signs of potential previous glacier collapses. Our analyses show that under specific circumstances climate variability and change have a critical potential to contribute to large-scale glacier instability by changing glacier geometry, thermal conditions and liquid-water content. Although long-term prediction of similar events seems beyond reach for the time being, the pre-event observations and simulations of the Aru-2 collapse demonstrate that available, state-of-the-art ground-based and satellite monitoring, and modelling capabilities allow for early warnings to be issued even in very remote regions. Harnessing these capabilities would allow for scientific advances to benefit also the most remote communities.

Methods

Methods, including statements of data availability and any associated accession codes and references, are available at https://doi.org/10.1038/s41561-017-0039-7.

References

1. Faillettaz, J., Funk, M. & Vincent, C. Avalanching glacier instabilities: Review on processes and early warning perspectives. *Rev. Geophys.* **53**, 203–224 (2015).
2. Huggel, C. Recent extreme slope failures in glacial environments: effects of thermal perturbation. *Quat. Sci. Rev.* **28**, 1119–1130 (2009).
3. Evans, S. G. et al. A re-examination of the mechanism and human impact of catastrophic mass flows originating on Nevado Huascaran, Cordillera Blanca, Peru in 1962 and 1970. *Eng. Geol.* **108**, 96–118 (2009).
4. Evans, S. G. & Delaney, K. B. in *Snow and Ice-related Hazards, Risks, and Disasters Hazards and Disasters Series* (eds Haeberli, W. & Whitemann, C.) 563–606 (Elsevier, Amsterdam, 2015).

5. van der Woerd, J. et al. Giant, ~M8 earthquake-triggered ice avalanches in the eastern Kunlun Shan, northern Tibet: characteristics, nature and dynamics. *Geol. Soc. Am. Bull.* **116**, 394–406 (2004).
6. Harrison, W. D. & Post, A. S. How much do we really know about glacier surging? *Ann. Glaciol.* **36**, 1–6 (2003).
7. Yasuda, T. & Furuya, M. Dynamics of surge-type glaciers in West Kunlun Shan, Northwestern Tibet. *J. Geophys. Res. F.* **120**, 2393–2405 (2015).
8. Harrison, W. D. et al. in *Snow and Ice-related Hazards, Risks, and Disasters Hazards and Disasters Series* (eds Haeberli, W. & Whitemann, C.) 437–485 (Elsevier, Amsterdam, 2015).
9. Sevestre, H. & Benn, D. I. Climatic and geometric controls on the global distribution of surge-type glaciers: implications for a unifying model of surging. *J. Glaciol.* **61**, 646–662 (2015).
10. Murray, T., Strozzi, T., Luckman, A., Jiskoot, H. & Christakos, P. Is there a single surge mechanism? Contrasts in dynamics between glacier surges in Svalbard and other regions. *J. Geophys. Res. B* **108**, 2237 (2003).
11. Jiskoot, H. in *Encyclopedia of Snow, Ice and Glaciers* (eds Singh, V. P. & Haritashya, U. K.) 415–428 (Springer, Dordrecht, 2011).
12. Fowler, A. C., Murray, T. & Ng, F. S. L. Thermally controlled glacier surging. *J. Glaciol.* **47**, 527–538 (2001).
13. Sevestre, H., Benn, D. I., Hulton, N. R. J. & Baelum, K. Thermal structure of Svalbard glaciers and implications for thermal switch models of glacier surging. *J. Geophys. Res. F.* **120**, 2220–2236 (2015).
14. Frappe, T. P. & Clarke, G. K. C. Slow surge of Trapridge Glacier, Yukon territory, Canada. *J. Geophys. Res. F.* **112**, F03s32 (2007).
15. Kamb, B. Glacier surge mechanism based on linked cavity configuration of the basal water conduit system. *J. Geophys. Res. B* **92**, 9083–9100 (1987).
16. Truffer, M., Harrison, W. D. & Echelmeyer, K. A. Glacier motion dominated by processes deep in underlying till. *J. Glaciol.* **46**, 213–221 (2000).
17. Clarke, G. K. C., Collins, S. G. & Thompson, D. E. Flow, thermal structure, and subglacial conditions of a surge-type glacier. *Can. J. Earth Sci.* **21**, 232–240 (1984).
18. Evans, S. G. et al. Catastrophic detachment and high-velocity long-runout flow of Kolka Glacier, Caucasus Mountains, Russia in 2002. *Geomorphology* **105**, 314–321 (2009).
19. Huggel, C. et al. The 2002 rock/ice avalanche at Kolka/Karmadon, Russian Caucasus: assessment of extraordinary avalanche formation and mobility, and application of QuickBird satellite imagery. *Nat. Hazard Earth Sys.* **5**, 173–187 (2005).
20. Haeberli, W. et al. The Kolka-Karmadon rock/ice slide of 20 September 2002: an extraordinary event of historical dimensions in North Ossetia, Russian Caucasus. *J. Glaciol.* **50**, 533–546 (2004).
21. Tian, L. D. et al. Two glaciers collapse in western Tibet. *J. Glaciol.* **63**, 194–197 (2017).
22. Heim, A. *Bergsturz und Menschenleben* (Fretz und Wasmuth, Zurich, 1932).
23. Chao, W. A. et al. Seismology-based early identification of dam-formation landquake events. *Sci. Rep.* **6**, 19259 (2016).
24. Christen, M., Kowalski, J. & Bartelt, P. RAMMS: Numerical simulation of dense snow avalanches in three-dimensional terrain. *Cold Reg. Sci. Technol.* **63**, 1–14 (2010).
25. Hungr, O. & McDougall, S. Two numerical models for landslide dynamic analysis. *Comput. Geosci.* **35**, 978–992 (2009).
26. Schneider, D., Huggel, C., Haeberli, W. & Kaitna, R. Unraveling driving factors for large rock-ice avalanche mobility. *Earth Surf. Process. Landf.* **36**, 1948–1966 (2011).
27. Yao, T. D. et al. Different glacier status with atmospheric circulations in Tibetan Plateau and surroundings. *Nat. Clim. Chang.* **2**, 663–667 (2012).
28. Ye, Q. H. et al. Glacier changes on the Tibetan Plateau derived from Landsat imagery: mid-1970s-2000-13. *J. Glaciol.* **63**, 273–287 (2017).
29. Brun, F., Berthier, E., Wagnon, P., Kaab, A. & Treichler, D. A spatially resolved estimate of High Mountain Asia glacier mass balances from 2000 to 2016. *Nat. Geosci.* **10**, 668–673 (2017).
30. Kääb, A., Treichler, D., Nuth, C. & Berthier, E. Contending estimates of 2003-2008 glacier mass balance over the Pamir-Karakoram-Himalaya. *Cryosphere* **9**, 557–564 (2015).
31. Berthier, E., Schiefer, E., Clarke, G. K. C., Menounos, B. & Remy, F. Contribution of Alaskan glaciers to sea-level rise derived from satellite imagery. *Nat. Geosci.* **3**, 92–95 (2010).
32. Tao, H., Borth, H., Fraedrich, K., Su, B. D. & Zhu, X. H. Drought and wetness variability in the Tarim River Basin and connection to large-scale atmospheric circulation. *Int. J. Climatol.* **34**, 2678–2684 (2014).
33. Kapnick, S. B., Delworth, T. L., Ashfaq, M., Malyshev, S. & Milly, P. C. D. Snowfall less sensitive to warming in Karakoram than in Himalayas due to a unique seasonal cycle. *Nat. Geosci.* **7**, 834–840 (2014).
34. Zhang, G. et al. Lake volume and groundwater storage variations in Tibetan Plateau's endorheic basin. *Geophys. Res. Lett.* **44**, 5550–5560 (2017).
35. Gruber, S. Derivation and analysis of a high-resolution estimate of global permafrost zonation. *Cryosphere* **6**, 221–233 (2012).
36. Boulton, G. S. & Jones, A. S. Stability of temperate ice caps and ice sheets resting on beds of deformable sediment. *J. Glaciol.* **24**, 29–43 (1979).
37. Cuffey, K. & Paterson, W. S. B. *The Physics of Glaciers* 4th edn (Butterworth-Heinemann, Burlington, 2010).
38. Kamb, B. Rheological nonlinearity and flow instability in the deforming bed mechanism of ice stream motion. *J. Geophys. Res. B* **96**, 16585–16595 (1991).
39. Tulaczyk, S., Kamb, W. B. & Engelhardt, H. F. Basal mechanics of Ice Stream B, West Antarctica 1. Till mechanics. *J. Geophys. Res. B* **105**, 463–481 (2000).
40. Iverson, N. R., Hooyer, T. S. & Baker, R. W. Ring-shear studies of till deformation: Coulomb-plastic behavior and distributed strain in glacier beds. *J. Glaciol.* **44**, 634–642 (1998).
41. Roering, J. J. et al. Beyond the angle of repose: A review and synthesis of landslide processes in response to rapid uplift, Eel River, Northern California. *Geomorphology* **236**, 109–131 (2015).
42. Dunse, T. et al. Glacier-surge mechanisms promoted by a hydro-thermodynamic feedback to summer melt. *Cryosphere* **9**, 197–215 (2015).
43. Fountain, A. G., Jacobel, R. W., Schlichting, R. & Jansson, P. Fractures as the main pathways of water flow in temperate glaciers. *Nature* **433**, 618–621 (2005).
44. Drobyshev, V. N. Glacial catastrophe of 20 September 2002 in North Osetia. *Russ. J. Earth Sci.* **8**, ES4004 (2006).
45. Chernomorets, S. S. et al. in *Debris-Flow Hazards Mitigation: Mechanics, Prediction, and Assessment* (eds Chen, C. L. & Major, J. J.) (Millpress, Rotterdam, 2007).
46. Zhang, W. Identification of glaciers with surge characteristics on the Tibetan Plateau. *Ann. Glaciol.* **16**, 168–172 (1992).
47. Ugalde, F., Casassa, G., Marangunic, C., Mujica, R. & Peralta, C. El deslizamiento catastrófico del glaciar Aparejo: 35 años después [In Spanish]. In *XiV Congresso Geologico Chileno* (Geological Society of Chile, La Serena, 2015); https://www.researchgate.net/publication/314207074_El_deslizamiento_catastrofico_del_glaciar_Aparejo_35_anos_despues
48. Heybrock, W. Earthquakes as a cause of glacier avalanches in the Caucasus. *Geogr. Rev.* **25**, 423–430 (1935).
49. Espizua, L. E. Fluctuations of the Rio-Del-Plomo glaciers. *Geogr. Ann. A* **68**, 317–327 (1986).
50. Milana, J. P. A model of the Glaciar Horcones Inferior surge, Aconcagua region, Argentina. *J. Glaciol.* **53**, 565–572 (2007).

Author contributions

All authors conceived the study, and collected, processed and analysed data. A.K., S.L., S.G., E.B., F.B., J.S.K., G.L. and D.T. performed remote-sensing analyses, A.G. performed mass-balance and thermo-dynamical glacier modelling, Y.B., P.B. and S.G.E. performed avalanche modelling, W.-A.C. and F.G. performed seismic data analysis and modelling, W.G., L.T., T.Y. and A.G. carried out field surveys and reconnaissance, and S.G.E., D.F. and C.H. performed further analyses and interpretations. All authors contributed to writing the paper.

Competing interests

The authors declare no competing financial interests.

Additional information

Supplementary information is available for this paper at https://doi.org/10.1038/s41561-017-0039-7.

Reprints and permissions information is available at www.nature.com/reprints.

Correspondence and requests for materials should be addressed to A.K.

Publisher's note: Springer Nature remains neutral with regard to jurisdictional claims in published maps and institutional affiliations.

Methods

Satellite remote sensing. Satellite data are critical to our understanding of the two Aru glacier collapses. Images from the Corona Cold War-era spy satellite programme over the period 1961–1980 are orthorectified using a rational function sensor model, and orthoimages and DEMs from 2015 WorldView and SPOT7 high-resolution optical satellite stereo data as reference[51] (Supplementary Section 1). Sensor-model residuals range over 8.6 to 15.2 m r.m.s. horizontally, for the different images respectively, but lateral offsets might be larger on glaciers where elevations changed significantly between acquisition dates and the DEMs, causing orthorectification offsets.

Satellite images of 1990–2017 from the Landsat 4–8 series, and Sentinel-2 data of 2016 are provided georeferenced and terrain corrected. Twenty-four-day repeat-pass Sentinel-1 radar images of 2014 until 2016 were geocoded using the ESA Sentinel tool box SNAP. The Planet cubesat constellation[52] consists of ~150–200 free-flying micro-satellites that carry RGB + NIR frame cameras that image the Earth surface in nadir direction with resolutions of 2–4 m (ref. [53]). Even if not yet complete in 2016, the Planet cubesat constellation covered the Aru area ~180 times in 2016 with completely or partially cloud-free images. The data used here are provided georeferenced and orthorectified.

DEMs from 2011 ALOS PRISM, 2015 WorldView and SPOT7, and 2016 Pleiades optical satellite stereo data are obtained from parallax matching using standard routines within the AMES Stereo Pipeline software[54] and PCI Geomatica[55]. For georeferencing, we use the orbital information provided but co-register the respective DEMs before computing DEM differences[56,57]. For stable ground, we obtain vertical differences between the 2015 WorldView and SPOT7 DEMs of ~2 m r.m.s. An assessment[58] of Pleiades DEMs over various mountain glaciers gave accuracies of better than ±1 m, and ±1.3 m for elevation differences between a Pleiades and SPOT5 DEM. We consider thus an accuracy of about ±2 m for individual pixels of our DEM differences to be conservative. Using an equally conservative distance of spatial error auto-correlation[59] of 400 m, we obtain thus standard errors of around ±0.8 m and ±0.9 × 10⁶ m³ for the elevation change and volume change of the collapse source areas, respectively, and around ± 0.1 m and ±0.8 × 10⁶ m³ for the avalanche deposits.

Monoscopic WorldView data of 2011 and 2013 are orthorectified using the 2015 Worldview DEM. Elevation differences between 2015 and 2011/2013 will lead to lateral orthorectification errors of only a few metres and have thus no significant impact on our results.

An estimate of glacier volume change rate is obtained from a time series of ASTER DEMs (Supplementary Section 7) following methods presented and validated earlier[29,60]. We generate 48 DEMs from ASTER AST_L1A images acquired between October 2000 and April 2015 using the Ames Stereo Pipeline[54]. All ASTER DEMs are corrected for planimetric and altimetric shifts and higher-order biases are corrected[29]. For each 30-m DEM pixel, we fit linear trends through the ASTER elevation values iteratively excluding outliers[29].

Based on bistatic TanDEM-X SAR data for 2011, 2013, 2014 and 2016, DEMs are produced using standard interferometric techniques (SLC stack co-registration, interferogram formation, topographic phase removal based on the SRTM DEM, phase unwrapping using the software SNAPHU, re-addition of SRTMSRTM DEM.derived topographic phase, phase to height conversion and geocoding). Absolute height calibration is done using Global Positioning System (GPS) field measurements. Linear trends in DEM differences and undulations (<5 m) contained in differences between the SRTM (February 2000) and the TanDEM-X DEMs are corrected by spatial extrapolation of height corrections estimated from stable terrain with low topography. Erroneous DEM values are removed for low interferometric coherence (TanDEM-X) and for height differences larger >10 m between the simultaneously acquired X- and C-band SRTM DEM.

To minimize effects of radar penetration, we do not use the C-band SRTM DEM, but rather the X-band SRTM DEM that covers the Aru range. The penetration of X-band radar waves is smaller than the one of C-band waves, and especially for differences between the TanDEM-X and SRTM-X DEMs, penetration effects are minimized when acquired under similar ground conditions. For such conditions, we estimate a maximum penetration depth difference of 1 m based on a conservative guess of 30% of the upper bound of 3 m penetration depth difference determined for a dry and a wet snow TanDEM-X DEM acquired in June and July 2011. On the basis of previous studies[61], tests on stable ground, and including the above penetration uncertainty, we estimate a total accuracy for individual DEM differences of ±2.6 m for SRTM/TanDEM-X and ±1.5 m for TanDEM-X alone.

The inundation by the Aru-1 lake impact wave was estimated from interferometric coherence loss within a pre/post-event Sentinel-1 image pair, from inspection of pre/post-event optical high-resolution images, and confirmed by GPS field survey. For interferometric change detection analysis, Sentinel-1 SLC data are processed using the tool box SNAP. For other visual analyses, GRD-format SAR data from Sentinel-1 are orthorectified on the basis of the SRTM-C DEM using PCI Geomatica and Google Earth Engine.

Event volumes. The volume estimates for the twin collapses are based on differencing DEMs from before (SRTM, TanDEM-X, ALOS PRISM World DEM, WorldView stereo and SPOT7 stereo) and after the events (Pleiades, TanDEM-X).

We differentiate between the collapse volumes (that is, the volume of the detached glacier parts) and the avalanche volumes (that is, the deposited volumes).

The raw DEM differences were corrected for the ice flux into the detached section of the glaciers that happened between the detachment date and the DEM date, for secondary smaller avalanches and for melt of the ice deposits on land and in the Aru Co lake (for Aru-1), and involved also density scenarios for the deposits (Supplementary Section 2).

From our above DEM accuracies, we conservatively estimate an uncertainty of the collapse volumes of ±0.8–0.9 × 10⁶ m³, while the small deviations between the DEM differences from the different before/after DEM combinations possible suggest an even higher accuracy. Further uncertainty stems from the above corrections of elevation changes between the detachment date and the date of Pleiades stereo acquisition (1 October 2016), in particular from partial closure of the detachment depression due to ice flux from the upper glacier parts and secondary avalanching or ice-debris erosion. We estimate the volume involved in these processes to amount up to 3 × 10⁶ m³ and attach a ±1 × 10⁶ m³ uncertainty to this number (Supplementary Section 2). Conservatively adding up the uncertainties from the DEMs and the volume changes after detachment, instead of using root-sum-square error propagation, leads to a total volume uncertainty for the collapses of roughly ± 2 × 10⁶ m³.

Reconciling the collapse volumes and the deposited avalanche volumes, the latter also obtained from DEM differencing, requires or provides, respectively, estimates for subaerial and aqueous melt (Aru-1), and deposit densities (Aru-1 and 2).

On the basis of the short time difference of ten days between the Aru-2 collapse and the Pleiades stereo acquisition, and air temperatures of around freezing suggested by ERA-interim data and snow fall in the region (from optical satellite data), we neglect melt of the Aru-2 deposits over these ten days. To roughly estimate the subaerial melt for the Aru-1 deposits between collapse and acquisition of the Pleiades data, we use a simple positive-degree day (PDD) approach based on meteorological and reanalysis data, neglect snow accumulation, and assume a range of PDD factors[62,63] comprised between 7.0 10⁻³ and 12.0 10⁻³ m w.e. K⁻¹ d⁻¹ (Supplementary Sections 3 and 5). The melt rates obtained agree with glaciological studies in central Tibet[64,65]. In further agreement, repeat GPS measurements over some points on the Aru-1 deposits between 13 August and 24 October 2016 suggest elevation loss of around 2.8 m.

DEM differencing over the Aru-2 deposits gives an avalanche volume of 102 × 10⁶ m³. Neglecting the evacuation of collapse and avalanche water content and sediment entrainment, and assuming the density difference between the detached (900 kg m⁻³ ice density) and deposited volume to be the only factor contributing to the volume differences, suggests a mean deposit density of 750 kg m⁻³, which seems reasonable for the ice melange deposited (Supplementary Section 2).

The Aru-1 deposits had a volume of 33–36 × 10⁶ m³ on 1 October 2016. Correction of this volume for aqueous melt in Aru Co (5.5 × 10⁶ m³), a density scenario of 750 kg m⁻³ as indicated for the Aru-2 collapse, and a rough 3 m w.e. melt scenario between 17 July and 1 October 2016, reconstructs, for instance, a collapse volume of around 72 × 10⁶ m³; that is, very close to the measured source volume of around 68 × 10⁶ m³ (Supplementary Section 2).

Climate and mass-balance calculations. We compare daily climate data from reanalysis and regional meteorological stations to estimate the climate in the Aru range since 1970. These data are used to model mass balance of the Aru glaciers based on a PDD model approach[66] that uses two distinct PDD factors for ice and snow, and takes into account the albedo feedback linked to precipitation increase. Downscaling of climate data to glacier scale is done assuming a constant lapse rate for temperature and precipitation. Furthermore, we apply a multiplicative factor to precipitation to correct a very likely bias in the precipitation[67]. We tune the model parameters to fit to mass balance as reconstructed from geodetic data (ICESat, TanDEM-X and ASTER) using a Bayesian probabilistic approach where the probability-density function is calculated by exploring the whole parameter space (Supplementary Section 3). From this procedure, we conclude that the ERA-interim reanalysis climate is able to explain the geodetic mass-balance observations in the Aru range sufficiently, mainly due to a precipitation increase since around 1995.

Thermal structure of the glaciers. The thermal structure of the Aru glaciers is simulated using a two-dimensional flow line of the southern Aru-2 glacier as an example (Aru-1 turns out to have a very similar structure). The bedrock topography is reconstructed on the basis of the post-event Pleiades DEM for the detached lower part, and using surface slope and a simple 'plastic approximation'[37] for the upper part, which has not collapsed. The model follows a published approach[68], solves the coupled Stokes and enthalpy equations, and takes into account meltwater percolation and refreezing in the firn and snow. The free-surface equation is used to compute geometrical change of the glacier surface by mesh deformation. Boundary conditions are determined by basal heat flux, surface temperature, surface melting and surface mass balance. The model is numerically solved by the finite-element software Elmer/Ice. The firn density is computed from the firn thickness given by the mass-balance model and assuming a linear density increase from the surface to the ice. We run the model using a constant

climate until it reaches a steady-state glacier. We apply a variety of parameter sets to evaluate the range of possible thermal regimes for the model glacier (Supplementary Section 9).

Seismic activity and analysis. We used the USGS earthquake catalogue to investigate whether significant ground motion from local earthquakes could have triggered the collapses of Aru-1 or Aru-2. Previous studies suggest that significant slope instability such as landslides may be triggered when peak ground acceleration exceeds a certain threshold, which was proposed[69] to be on the order of $1\,m\,s^{-2}$. Considering that this threshold value also applies to a glacier collapse, significant glacier destabilization would require a local ($<10\,km$ distance) earthquake with magnitude equal to or larger than 4, a distant ($<100\,km$) earthquake with magnitude equal to or larger than 6 or a very distant ($<1,000\,km$) earthquake with magnitude equal to or larger than 8 (ref. [70]). Within months prior to the Aru glacier collapses, there were no magnitude>8 earthquakes observed within $1000\,km$ from the Aru glacier site, as well as no magnitude>6 and >4 earthquakes within 100 and $10\,km$, respectively (Supplementary Section 10). Over the past seven years, seismicity within $100\,km$ from the Aru glaciers has been limited to about a dozen of magnitude 4–5 earthquakes, none of which particularly close in time to the Aru collapses. The most significant peak acceleration values prior to the collapses were due to a magnitude 4.1 earthquake that occurred at ~$10\,km$ distance on 16 December 2015, six months prior to the Aru-1 collapse and five months after Aru-1 started advancing. Thus, it is very unlikely that either of the collapses was triggered by earthquakes.

The avalanche-induced seismic waves and our seismic source inversions based on them are outlined in Supplementary Section 10.

Geothermal activity. The local population in the Aru region mentions the existence of warm springs $15\,km$ north of the Aru glaciers. We consulted a number of ASTER and Landsat thermal imagery of all seasons but were unable to detect any clear indication of abnormal geothermal surface heat flux close to the glaciers, in the detachment zone, or anywhere near the area. However, the combination of low spatial resolution of the thermal bands used (60–90 m) with the rough topography and variable snow and ice cover would make such detection of small surface heat-flux anomalies uncertain. Also inspection of high-resolution satellite images over the exposed glacier bed gives no conclusive indications about potential sources of significantly increased geothermal heat flux. We identify, though, some spots around the glaciers that could be examined closer in the field with respect to abnormal geothermal heat flux, such as a hollow in the ice at one place at the margin of the Aru-2 glacier, but not in proximity to the detached glacier part. Strongly reduced backscatter between repeat TerraSAR-X data over winter 2016/2017 indicates some small outflows of liquid water in the avalanche zone despite of freezing conditions.

Lithology. Non-public geological maps of the Aru region were made available for inspection. They indicate a dominance in the Aru Range of un-metamorphosed or lightly metamorphosed fine-grained Permian sedimentary rocks, especially sandstone, siltstone, slate and conglomerate; some nearby glacierized ranges contain similar lithologies, but all other glacierized ranges also contain lithologies not present in the Aru Range, including metamorphosed schist and phyllite equivalents of rocks already mentioned, plus limestone, dolomite, massive conglomerate and biotite granite. The fine-grained sedimentary rocks (or low-medium-grade equivalents) were confirmed for the avalanche zones during a field visit in July 2017, when we also collected extruded clay-rich till (Supplementary Section 12).

To better constrain spatial patterns of surface lithological variations, we employ a 10 September 2015 cloud- and snow-free pre-avalanche Landsat 8 Operational Land Imager (OLI) surface reflectance image[71]. Cells containing significant vegetation, water or snow are identified and masked out, and the remaining cells represent mostly rock and sediment. Thirty alluvial deposit areas-of-interest are defined from the Aru and adjacent ranges, each emanating from a discrete glacier terminus (Supplementary Section 12). Care is taken to avoid lithologic cross-sampling from sediment feeding from adjacent glacier systems that intersect the targeted alluvium. Surface reflectance and selected band ratios are tabulated for OLI bands 1–7 in each of the 30 glacier-fed alluvial deposits. These band ratios[72,73] are used here to identify spectral clusters that may pertain to distinct lithologies.

Uncertainties. Our measurements and data include a range of uncertainties as summarized in the following. For precipitation data, the exact precipitation over the Aru glaciers is uncertain but meteorological stations, GPM IMERG data and local reports agree about the particularly high precipitation rates in 2016 and several previous years. Similarly, while yearly rates of precipitation change differ, an increase in precipitation of 5–7 mm $10\,yr^{-1}$ in the region over the past 3–4 decades is a robust finding across the data sets and furthermore supported by analyses of the pronounced growth of endorheic lakes[34,74,75].

Uncertainties in glacier length, elevation and volume changes, glacier surface velocities and Aru lake impact wave run-up are low and well understood from consistent results from multiple independent measurements and from published method validations. Glacier length errors are in the range 1–60 m depending

on the sensor used, elevation is within ± 1 to $\pm 5\,m$ (TanDEM-X and SRTM, respectively), glacier surface velocities are within ± 0.01–$0.05\,m\,d^{-1}$ (WorldView and Sentinel-2), and wave run-up is within $\pm 20\,m$ horizontally (Sentinel-1; better for Planet and GPS).

For avalanche speed and characteristics, the high avalanche speeds are confirmed by both local reports and seismic data. High initial avalanche water content is corroborated by high precipitation and, in particular, melt rates found weeks before the events by observations in radar and optical satellite images.

For thermal and soft-bed glacier conditions, the existence of cold-based glacier fronts and margins is supported by thermal modelling using a wide range of plausible parameter sets, and by the geographic setting of the study area in a permafrost region[35,76]. The main uncertainty remains in the existence of basal temperate ice in the accumulation area. The unbalanced mass transfer observed from surface height change suggests the presence of temperate basal ice at least after 2010. The presence of fine-grained glacier beds is confirmed by a specific field visit in July 2017, which revealed large amounts of silt/clay in the upper avalanche path of Aru-1. Such soils are known to have a strong impact on the motion of glaciers[38–40] and on landsliding[41].

Overall, our main conclusions remain robust against the identified and quantified uncertainties. Rather than a single factor, a rare transient array of factors combined to both increase shear stress and reduce shear strength, eventually resulting in failure. The relative importance of these factors can hardly be quantified, which is a common conclusion in other slope failure studies in high mountains[77,78], and in particular a natural consequence of the rareness of the events studied here. The uniqueness of the events is confirmed by: the dense satellite data time series, which does not indicate similar collapses in the Aru Range and the range north of it since 1961, and since 1972 for the whole western Tibetan Plateau (~300 km radius around Aru); and testimonies of local herders who do not recall any similar event.

Data availability. Publicly available remote-sensing data sources used in this study include Sentinel-1 and 2, available from https://scihub.copernicus.eu/, Landsat, SRTM-C and Corona, available from http://earthexplorer.usgs.gov, ASTER, available from https://reverb.echo.nasa.gov/, SRTM-X from http://eoweb.dlr.de, and GPM IMERG, available from https://pmm.nasa.gov/. Pleiades data are commercial but academic access exists through ISIS (http://www.isis-cnes.fr/). WorldView and SPOT7 data are commercial. Planet data are commercial but academic access schemes exist (https://www.planet.com/products/education-and-research/). TerraSAR-X and TanDEM-X data are available via http://eoweb.dlr.de free of charge via scientific proposals. Seismic records are publicly available from http://www.iris.edu, and earthquake data from https://earthquake.usgs.gov/.

Code availability. The image correlation code CIAS is available from http://mn.uio.no/icemass. The AMES stereo-pipeline code is available from https://ti.arc.nasa.gov/tech/asr/groups/intelligent-robotics/ngt/stereo/. The SNAP remote-sensing toolbox can be downloaded from http://step.esa.int/ and Elmer/Ice can be downloaded from http://elmerice.elmerfem.org/.

References

51. Sorg, A., Kääb, A., Roesch, A., Bigler, C. & Stoffel, M. Contrasting responses of Central Asian rock glaciers to global warming. *Sci. Rep.* **5**, 8228 (2015).
52. Kääb, A., Altena, B. & Mascaro, J. Coseismic displacements of the 14 November 2016 Mw 7.8 Kaikoura, New Zealand, earthquake using the Planet optical cubesat constellation. *Nat. Hazard Earth Sys.* **17**, 627–639 (2017).
53. Planet Team. *Planet Application Program Interface: In Space for Life on Earth* (San Francisco, CA, accessed 17 December 2016); https://api.planet.comhttps://www.planet.com
54. Shean, D. E. et al. An automated, open-source pipeline for mass production of digital elevation models (DEMs) from very-high-resolution commercial stereo satellite imagery. *ISPRS J. Photogramm.* **116**, 101–117 (2016).
55. Kronenberg, M. et al. Mass-balance reconstruction for Glacier No. 354, Tien Shan, from 2003 to 2014. *Ann. Glaciol.* **57**, 92–102 (2016).
56. Nuth, C. & Kääb, A. Co-registration and bias corrections of satellite elevation data sets for quantifying glacier thickness change. *Cryosphere* **5**, 271–290 (2011).
57. Berthier, E. et al. Remote sensing estimates of glacier mass balances in the Himachal Pradesh (Western Himalaya, India). *Remote. Sens. Environ.* **108**, 327–338 (2007).
58. Berthier, E. et al. Glacier topography and elevation changes derived from Pleiades sub-meter stereo images. *Cryosphere* **8**, 2275–2291 (2014).
59. Wang, D. & Kääb, A. Modeling glacier elevation change from DEM time series. *Remote. Sens.* **7**, 10117–10142 (2015).
60. Berthier, E., Cabot, V., Vincent, C. & Six, D. Decadal region-wide and glacier-wide mass balances derived from multi-temporal ASTER satellite digital elevation models. Validation over the Mont-Blanc area. *Front. Earth Sci.* **4**, 63 (2016).
61. Round, V., Leinss, S., Huss, M., Haemmig, C. & Hajnsek, I. Surge dynamics and lake outbursts of Kyagar Glacier, Karakoram. *Cryosphere* **11**, 723–739 (2017).

62. Kayastha, R. B. et al. Positive degree-day factors for ice ablation on four glaciers in the Nepalese Himalayas and Qinghai-Tibetan Plateau. *Bull. Glaciol. Res.* **20**, 7–14 (2003).

63. Gao, H. K., He, X. B., Ye, B. S. & Pu, J. C. Modeling the runoff and glacier mass balance in a small watershed on the Central Tibetan Plateau, China, from 1955 to 2008. *Hydrol. Process.* **26**, 1593–1603 (2012).

64. Mölg, T., Maussion, F., Yang, W. & Scherer, D. The footprint of Asian monsoon dynamics in the mass and energy balance of a Tibetan glacier. *Cryosphere* **6**, 1445–1461 (2012).

65. Caidong, C. D. & Sorteberg, A. Modelled mass balance of Xibu glacier, Tibetan Plateau: sensitivity to climate change. *J. Glaciol.* **56**, 235–248 (2010).

66. Gilbert, A. et al. Sensitivity of Barnes Ice Cap, Baffin Island, Canada, to climate state and internal dynamics. *J. Geophys. Res. F.* **121**, 1516–1539 (2016).

67. Immerzeel, W. W., Wanders, N., Lutz, A. F., Shea, J. M. & Bierkens, M. F. P. Reconciling high-altitude precipitation in the upper Indus basin with glacier mass balances and runoff. *Hydrol. Earth Syst. Sci.* **19**, 4673–4687 (2015).

68. Gilbert, A., Gagliardini, O., Vincent, C. & Wagnon, P. A 3-D thermal regime model suitable for cold accumulation zones of polythermal mountain glaciers. *J. Geophys. Res. F.* **119**, 1876–1893 (2014).

69. Wang, X., Nie, G. & Wang, D. Relationships between ground motion parameters and landslides induced by Wenchuan earthquake. *Earthq. Sci.* **23**, 233–242 (2010).

70. Liu, K. S. & Tsai, Y. B. Attenuation relationships of peak ground acceleration and velocity for crustal earthquakes in Taiwan. *Bull. Seismol. Soc. Am.* **95**, 1045–1058 (2005).

71. Vermote, E., Justice, C., Claverie, M. & Franch, B. Preliminary analysis of the performance of the Landsat 8/OLI land surface reflectance product. *Remote. Sens. Environ.* **185**, 46–56 (2016).

72. Ashley, R. P. & Abrams, M. J. Mapping of limonite, clay mineral, and alunite contents of hydrothermally altered rocks in cuprite mining district, Nevada, using aircraft scanner imagery for 0.46-2.36 µm spectral region. *Econ. Geol.* **73**, 307–307 (1978).

73. Mwaniki, M. W., Matthias, M. S. & Schellmann, G. Application of remote sensing technologies to map the structural geology of Central Region of Kenya. *IEEE J. -Stars* **8**, 1855–1867 (2015).

74. Song, C. Q., Huang, B. & Ke, L. H. Heterogeneous change patterns of water level for inland lakes in High Mountain Asia derived from multi-mission satellite altimetry. *Hydrol. Process.* **29**, 2769–2781 (2015).

75. Zhang, G. et al. Extensive and drastically different alpine lake changes on Asia's high plateaus during the past four decades. *Geophys. Res. Lett.* **44**, 252–260 (2017).

76. Ran, Y. H. et al. Distribution of permafrost in China: an overview of existing permafrost maps. *Permafr. Periglac.* **23**, 322–333 (2012).

77. Fischer, L., Amann, F., Moore, J. R. & Huggel, C. Assessment of periglacial slope stability for the 1988 Tschierva rock avalanche (Piz Morteratsch, Switzerland). *Eng. Geol.* **116**, 32–43 (2010).

78. Phillips, M. et al. Rock slope failure in a recently deglaciated permafrost rock wall at Piz Kesch (Eastern Swiss Alps), February 2014. *Earth Surf. Process. Landf.* **42**, 426–438 (2017).